The effect radar imaging of astroids by migration of slant stacked data

Victor Savenije
Utrecht University

Supervised by Ivan Vasconselos

April 2, 2018

Abstract

The structure of asteroids remains ill-unknown due to few effective methods to accurately image their interior. In this paper, using a synthetic model of an asteroid, radar imaging by migration of slant stacked data is studied. The basis for this method relies on beamforming in the electric wavefield due to the interference of pointsource responses. This method, here referred to as waveform Synthetic Aperture Radar (SAR) imaging, is evaluated for migration at both the source- and receiver-side, but results are very comparable. Waveform SAR is compared to imaging with zero-offset data as well as multi-offset data, the latter only acquirable by using more than one satellite in practice. Waveform SAR shows better image quality than zero-offset data migration when the target is coarsely spatially sampled by data points. This is because the image using

waveform SAR is more accurate per shot, due to amplification of signal near the true location of scatterers.

Contents

1 Introduction

Asteroids are of scientific value, because they give evidence of the composition, collisional and thermal evolution of the early solar system. The interior structure of asteroids may provide clues about their evolution, and that of the solar system with respect to differentiation, impacts and reassembly (Sava et al, 2014; Bottke et al, 2002). Near-Earth Asteroids (NEAs) are also of great interest because of their possible collision risk with the Earth (Chapman 2004). Moreover, there is increasing economic interest in asteroids because of future mining possibilities (Graps et al. 2016).

However, currently, very little is known about asteroids interiors. Although there have been various missions to asteroids or comets (e.g.: Deep space 1, HAYABUSA, Deep Impact), most scientific experiments only provide information about the asteroid to a very limited depth (e.g. the crator left by the Deep Impact mission is estimated to be about 30 meter deep (A'Hearn et al)).

Imaging using propagating waves, in contrast to field methods such as gravimetry, is one of the few ways to retrieve better resolution at depth inside asteroids, thus allowing for better interpretation of their internal properties. One such technique would be seismic imaging, but because of its requirement for mechanical contact with the asteroids would pose significant practical challenges, this paper will focus on the potential use of non-contacting radar imaging. Reflection, and potentially transmission-based radar imaging should map dielectric contrasts inside the asteroid which correspond with the asteroid structure (Safaeinili et al, 2002). Although this radar imaging technique is used regularly on Earth for a variety of applications, it has never been done targeting an asteroid, although the ROSETTA mission did preform a transmission experiment on a comet (the CONSERT experiment) using a lander and orbiter (Kofman et al. 2015). However, with this limited setup, the internal structure could not be inferred, instead only general information about the comet interior can be stated.

Radar reflection imaging has been preformed on Mars by mission experiments such as MARSIS (Jordan et al, 2009) and SHARAD (Sue et al, 2007). But an important difference is that the satalites orbiting an asteroid can be located much closer to the surface than the satelites orbiting Mars. For example the closest approch at periapsis was at 250km for the MARSIS expriment (Jordan et al, 2009).

Image quality can be increased by an aquisition using two orbiters, rather than a single orbiter that emits and records the electromagnetic (EM) waves (Sava et al, 2014; Grimm et al, 2014; Detchai Ittharat 2014). Data is than said to inhibit variable shot-receiver distance, or off-set. However, this very expensive method requires (at least) two satellites.

An alternative, less expensive way to increase image quality may be to use beamforming of the EM waves by combining multiple sources/recording locations. This can be done by slant stacking data from multiple locations. This

setup using multiple point sources reflects an experiment that uses e.g. a radar dish to record and/or emit EM waves. Both proccesing on the source (directional emitting of EM waves) or the receiver side (directional amplifying of recorded EM waves) can be used to increase image quality.

In the context of seismics and ground penetrating radar (GPR), a very similar data processing technique involving time-delaying and stacking data originating from point sources (*slant stacking*) is referred to as the τ-p transform (Stoffa et al. 1981). Images made by plane-wave migration using the data from the τ-p domain, benefit from a decrease in computational cost and/or removal of artifacts caused by multiples (Stoffa et al. 2006).

A similar processing technique, referred to as Synthetic Aperture Radar, is employed in the context of imaging of the earth from plane or satellite. However this relatively 'far-field' method is different from GPR. The shape and arrival time of the first arrivals are considered instead of the whole waveform that is recorded after the initial arrival, in contrast to seismics and GPR (Skolnik, 1970).

In this research where GPR targeting asteroids from satellites is discussed, I investigate whether the slant stacking data processing can be used to improve the imaging of asteroid interiors. Because of the similarities to both GPR and SAR, I will refer to this as *waveform SAR*.

2 Methods

In order to explore the effect of waveform Synthetic Aperture Radar (waveform SAR) on image quality, images are produced from data originating from a synthetic model. Images are made using reverse time migration (RTM) (Baysal et al. 1983) and different acquisitions are compared to each other. Therefore, this paper is outlined in the following way: the theoretical basis for wavefield modelling will be discussed first because RTM requires computation of wavefields. Next, model setup considerations will be discussed, and after that the imaging theory will be presented. Then, waveform SAR will be discussed, and it's results evaluated.

2.1 Wavefield modelling

In this section, I explain the the wave operator used in this paper, and under which conditions it can be used to image asteroids. An electromagnetic field can be described by the coupled vector quantities electric and magnetic field. The intensity of the decoupled electric field is given by the Telegraph equation (Griffiths, 2008):

$$\nabla^2 E - \mu\epsilon\frac{\partial^2 E}{\partial t^2} - \mu\sigma\frac{\partial E}{\partial t} = 0 \tag{1}$$

Here, E is the electric field intensity, μ is the magnetic permeability, ϵ is the electric permittivity and σ the conductivity. Equation (1) represents a wave equation with a wavespeed $v = \sqrt{\epsilon\mu}$. The wave speed is thus controlled by electric permittivity (ϵ) and magnetic permeability (μ).

In reality, the magnetic and electric field are vectors, and therefore the wave equation may have a polarity. Thus, accurate modeling of wave propagation may consider this polarity, however, in this paper a scalar wave equation will be used as presented in equation 1, thus only considering the intensity of the fields. This is possible because the waves travel with the same kinematics as the vector wave equation under the assumption that polarity changes at interfaces are relatively small.

High conductivity leads a higher contribution of the dissipative term in the wave equation $-\mu\sigma\frac{\partial \mathbf{E}}{\partial t}$. The influence of this attenuation on the imaging of asteroids is probably large and is further explored by Grimm et al (2014). However, in this paper I will not include this dissipative term. Thus the wave equation used in this paper, by additionally inserting $v = \sqrt{\epsilon\mu}$, is:

$$\nabla^2 E - v^2\frac{\partial^2 E}{\partial t^2} = 0 \tag{2}$$

To model wave propagation numerically, the wave equation is discretised using finite differences, introducing a fixed time-step Δt (Ladyzhenskaya, 1985). The double time derivative term in the wave equation is then formulated in the following way:

$$\frac{\partial^2 E(t)}{\partial t^2} = \left(\frac{E(t+\Delta t) - 2E(t) + E(t\text{-}\Delta t)}{(\Delta t)^2} \right) \tag{3}$$

By rewriting this equation, the future electric field $E(t+\Delta t)$ can be formulated by the previously calculated electric fields $E(t\text{-}\Delta t)$ and $E(t)$. In the wave modelling used in this paper, the spatial derivative term $\nabla^2 E$ in the wave equation (1) is similarly discretised (using an higher order finite difference scheme to enhance the stability of the numerical solution). The finite difference scheme presented here is used to simulate wavefields, needed to perform RTM on the data originating from a synthetic asteroid model.

2.2 Model setup

In order to asses the quality of images, I assume an initial model. The model is chosen based on a 2-dimensional cross-section through the shape of asteroid Eros 433, but the size of the model is scaled down to fit inside a rectangle of 1000 by 500 meters. This shape is inspired by the work of Sava (2014). The wave speed within the asteroid is also chosen based on their work. The theoretical basis for the wave speed relies on the idea that the velocity relates to density. A realistic mean density of 2.0 g/cm^3 for asteroids is chosen. However, the asteroid is also assumed to inhibit a structure of regolith and rocky material, which are chosen to have densities of 1.0 and 3.0 g/cm^3 respectively. Based on an empirical relation, ($\epsilon' = \epsilon_r/\epsilon_0 = 1.93^\rho$), an relative electric permittivity can be inferred. A constant magnetic permeability μ is assumed across the whole imaging domain, set to be the magnetic permeability of space (1.25 μH/m). The resulting velocity in the medium is then given by $v = (\mu_0 \cdot \epsilon_r)^{0.5}$. This is summarized in the table 1, and the actual velocity model is shown in figure 1.

Table 1: Model parameters for the 3 media in the synthetic velocity model

	ρ (g/cm^3)	ϵ' (-)	v (m/ns)
Space	0	1	0.33
Regolith	1	1.93	0.22
Rock	3	6.86	0.11

The electromagnetic impulse, the source, is chosen be a Ricker wavelet with a center frequency of 10 MHz. The choice of this frequency will greatly influence results in practice, because the frequency effects the amount of attenuation (Grimm et al 2014). In this study 10 MHz will be used because it is in the range of what actual satellite based sources can produce (Safaeinili et al. 2002), it is between the frequencies used by MARSIS (Jordan et al, 2009) and SHARAD experiment (Sue et al, 2007), and it is comparable to the work of Detchai Ittharat (2014) and Sava et al (2014).

In order to generate data with high enough spatial sampling, the electromagnetic impulse is emitted and recorded at a large amount of points in a ring

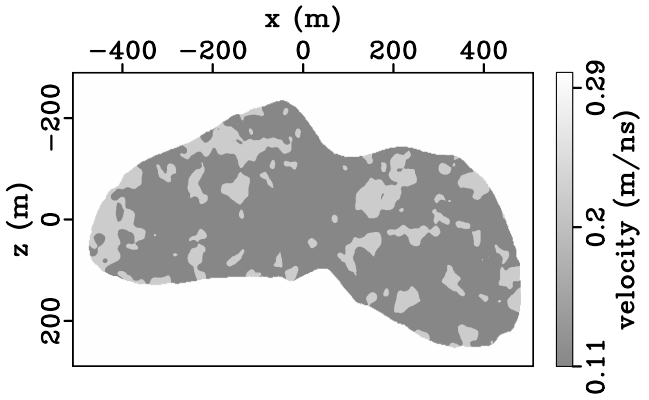

Figure 1: Velocity model. Based on the work of Sava (2014) (scaled down version of Eros 433). Model resembles 3 media (Space, rock and regolith), that are distributed randomly.

around the asteroid, separated by a constant distance. I choose a sampling of 5 points per wavelength in space ($\lambda \approx 30m$), which results in a spatial distance of $\big(30/5\big) \approx 6$ meters. The radius of the location ring is about 100-400 meters above the asteroid surface. The acquisition setup with the ring of locations is shown in figure 3.

In case there is only one orbiter, the receiver location is the same as the source location, because the wave velocities are much larger than the orbit velocity. The data produced by this acquisition is referred to as *zero-offset* data. In case there are 2 (or more) orbiters, data can be recorded at multiple offsets, ideally at all locations in a full ring around the asteroid. I will refer to this as a *full acquisition* design. In the migration results section I will show the results of both this ideal full acquisition case as well as the result of zero-offset data in order benchmark images using SAR.

In this study we are interested in scatters within the asteroid. To account for this, arrivals originating from a background model are subtracted from the data produced by the true model. This background model has constant velocity within the asteroid. By doing this, the direct arrival is partly discarded: the first reflection of the asteroid surface is attenuated. The resulting zero-offset data is visualized in figure 2.

2.3 Migration

In this paper, reverse time migration (RTM) is employed (Baysal et al. 1983). This imaging method relies on wavefield reconstruction, and an imaging condition. In section 'Wavefield modelling', I discussed the wave equation (eq. 2) that governs the wavefield reconstruction. The operator $\mathbf{L}$ that describes this wavefield is then defined as:

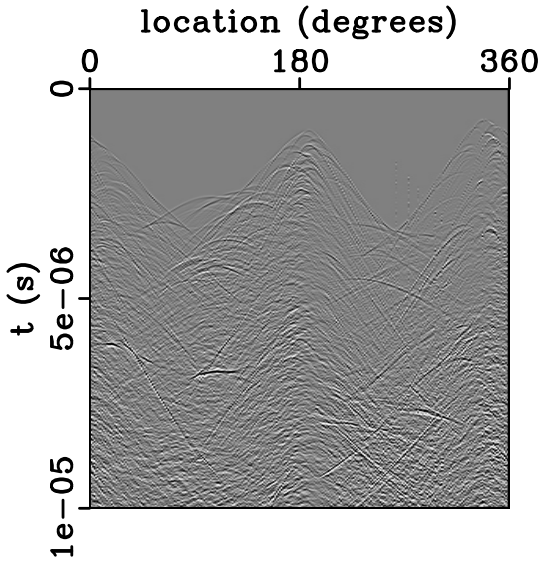

Figure 2: Zero-offset data, shown with a gain of factor t. Location as defined in figure 3 by an angle α

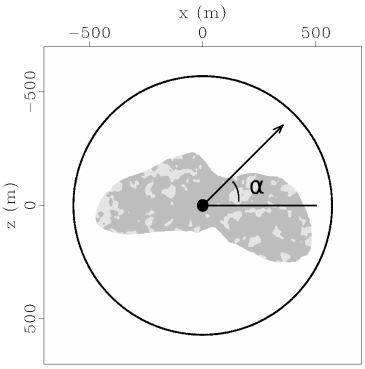

Figure 3: Acquisition ring.

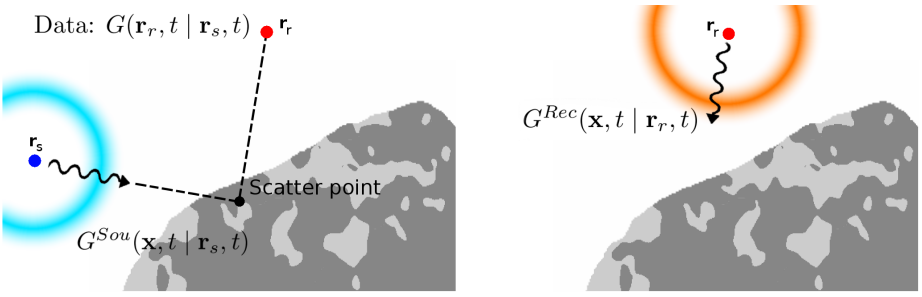

(a) Source side

(b) Receiver side

Figure 4: Illustration schematically showing a source location $\mathbf{r}_s$, receiver location $\mathbf{r}_r$, source wavefield $G^{Sou}(\mathbf{x}, t)$, recorded data $G(\mathbf{r}_r, t \mid \mathbf{r}_s, t)$ and receiver wavefield $G^{Rec}(\mathbf{x}, t \mid \mathbf{r}_r, t)$

$$\mathbf{L}\big(v(\mathbf{x})\big)[G] = \nabla^2 G(\mathbf{x},t) - v^2(\mathbf{x})\frac{\partial^2 G(\mathbf{x},t)}{\partial t^2} = f(\mathbf{x},t) \tag{4}$$

Here, $G(\mathbf{x},t)$ is the wavefield, $v(\mathbf{x})$ is the wavespeed and $f(\mathbf{x},t)$ represents the source wavelet, emitted at location(s) $\mathbf{x}$ and time t. With this wave operator, I reconstruct the *source-* and *receiver wavefield*. The source wavefield G^{Sou} depends on the source wavelet $S(\mathbf{r}_s,t)$ by operator $\mathbf{L}$:

$$\mathbf{L}\big(v_{mig}\big)[G^{Sou}(\mathbf{x},t)] = S(\mathbf{r}_s,t) \tag{5}$$

Here, v_{mig} is the assumed velocity model for migration, and $\mathbf{r}_s$ represents the source location. The receiver wavefield depends on the data $D(\mathbf{r}_r,t)$, measured by recording location(s) $\mathbf{r}_r$ by the following similar equation:

$$\mathbf{L}\big(v_{mig}\big)[G^{Rec}(\mathbf{x},t)] = D(\mathbf{r}_r,\text{-}t) \tag{6}$$

The receiver wavefield is propagated backwards in time, until the moment the recording was started, and thus both wavefields span the same time interval. Differences in the source- and receiver wavefield are caused by an incorrect assumed velocity model or incomplete data coverage.

The imaging condition chosen is this paper is the zero-lag cross-correlation between the source and reversed receiver wavefield (Claerabout 1985):

$$Im(\mathbf{x},\mathbf{r}_r,\mathbf{r}_s) \propto \Big[G^{Sou}(\mathbf{x},t) * G^{Rec}(\mathbf{x},\text{-}t)\Big]_{t=0} \tag{7}$$

The corresponding discrete formulation of this in the time-domain is:

$$Im(\mathbf{x},\mathbf{r}_r,\mathbf{r}_s) = \sum_t G^{Sou}(\mathbf{x},t)\cdot G^{Rec}(\mathbf{x},\text{-}t) \tag{8}$$

The image is thus the multiplication of the source and receiver wavefields, $G^{Sou}(\mathbf{x},t)$ and $G^{Rec}(\mathbf{x},t)$, stacked over each time step. Image quality is then further improved by summing the image over all shots points.

For better visualization of the scattering contacts, the image results are sharpened and clipped. Sharpening enhances the projection of scattering contacts because the true model only includes scatters originating from sharp velocity contrasts. Figure 5 shows the results using the RTM method as outlined above. The figures use data, shot & recorded by the locations denoted by the ring in figure 3. Left side figures A & C use the true velocity model for migration, while right-side figures B & D use an less accurate velocity model denoted by the name Asteroid-shape. This Asteroid-shape model assumes a constant velocity inside the asteroid, the magnitude of the velocity is the average of the 2 media in the true velocity model. The top two figures A & B use zero-set data, as visualized in 2. In contrast, the lower two figures use full acquisition data.

The large difference in image quality in figures 5 illustrate the artifacts that appear when using an incorrect velocity model and/or zero-offset data. Artifacts originating from multipathing are probably strongly present when preforming

experiments targeting asteroids because asteroids are thought to inhibit large velocity variations (Safaeinili et al, 2002). Multi-offset data allows attenuation of artifacts caused by multipathing (Claerbout, 1985; Sava et al, 2014). Sava et al. demonstrates that with increasing offset in the data, the image quality improves greatly. This is also clearly apparent by the difference in quality of top & bottom in figure 5. However, multi-offset data can only be acquired in practice by the expensive acquisition of (at least) 2 orbiters.

2.4 Waveform SAR

In this research, I investigate whether waveform Synthetic Aperture Radar (*waveform SAR*) as presented in the introduction can be used to improve the image quality. For clarity, in the context of this paper where I discuss ground-penetrating radar targeting asteroids from satellites, waveform SAR is referred to as the technique of gaining extra information based on multiple shot/receiver locations. The basis is the interference of wavefields originating from multiple pointsources leading beamforming. Waveform SAR can be used on both source and receiver side. I will first consider source-side waveform SAR, though both options will be presented in this paper.

2.4.1 Source-side

The data of source-side waveform SAR is produced by emitting an electromagnetic source in a certain direction, instead of using the response of a point source. In practice this directional source can emitted by various instruments which influence the source wave geometry accordingly. I will represent this directional source by using a set of point sources in a nearly straight line, referred to as $\mathbf{r}_p$. This is the source array, that each fire with a slight delay (a phased array). The recording point located in the middle of this array is refered to as $\mathbf{r}_r$. Figure 6 shows this setup.

The total wavefield originating from multiple sources is the sum of all the wavefields originating from each source because the wave propagation operator, stated in equation 10, is linear. Using this linearity, I can produce this slant stacked data by using a subset of the recorded data of a full acquisition setup (multi-offset data with perfect coverage). This is done by time-shifting and stacking the data, shot at the locations in an array with in the middle the recorder point, which is referred to as slant stacking. This formulated in the following equation:

$$D_s(\mathbf{r}_r, \beta) = \sum_p G_p\big(\mathbf{r}_r, t \mid \mathbf{r}_p,\ t{+}\Delta t_{p,\beta}\big) \tag{9}$$

Here, D_s is the source-side, slant stacked data for a location $\mathbf{r}_s$, and angle β. p represents the point sources inside the source array. $\Delta t_{p,\beta}$ shifts the data in time; the magnitude of the time-shift depends on angle β and source point $\mathbf{r}_p$. $G_p\big(\mathbf{r}_s, t \mid \mathbf{r}_p,\ t{+}\Delta t_{p,\beta}\big)$ is then the data trace recorded at location $\mathbf{r}_s$, shot

(a) V_{model} True

(b) V_{model} Asteroid-shape

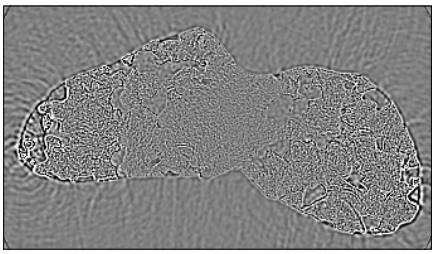

(c) V_{model}: True, Data: zero-offset

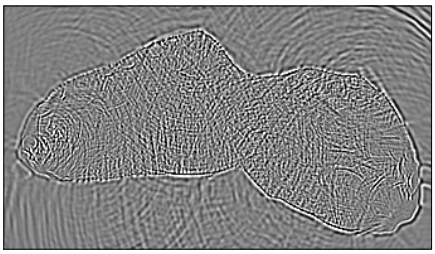

(d) V_{model}: Asteroid-shape, Data: zero-offset

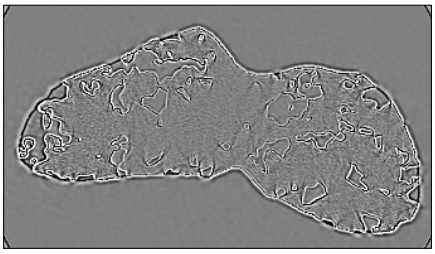

(e) V_{model}: True, Data: full acquisition

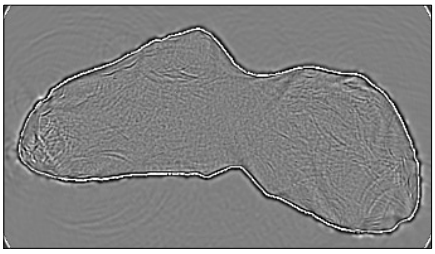

(f) V_{model}: Asteroid-shape, Data: full acquisition

Figure 5: Benchmark images. Indicated is the used velocity model for migration, and the data. Data either zero-offset, refering to aquisition by a single orbiter, or multi-offset data with perfect coverage, referred to as full acquisition. For magnitude of the velocity model & scale, see figure 1.

by a point source at the location $\mathbf{r}_p$, and shifted in time by $\Delta t_{p,\beta}$. The time shift $\Delta t_{p,\beta}$ is formulated as:

$$\Delta t_{p,\beta} = \left(\mathbf{r}_p\text{-}\mathbf{r}_r\right) \cdot \frac{sin(\beta)}{v_{space}} \tag{10}$$

Where $\left(\mathbf{r}_p\text{-}\mathbf{r}_r\right)$ is the distance between the point source location and recorder location, β denotes the direction of maximum amplitude (see figure 6), and v_{space} is the velocity in space. The time shift Δt is linearly dependent on the distance from the recorder point $\mathbf{r}_r$ at the center of the point source array $\mathbf{r}_p$, to the individual point source $\mathbf{r}_p$. By this slant stacking procedure, the data by equation 10, the data represents the measurement if the source wave is directional (see figure 6).

By further adjusting the time axis accordingly, one can focus the source beam at a certain distance. In this paper, the source points are not on a straight line, but rather on a circle around the asteroid. By this geometry, the source beam will be focused on the middle of the target. Further adjusting of the focus will not be considered in this paper.

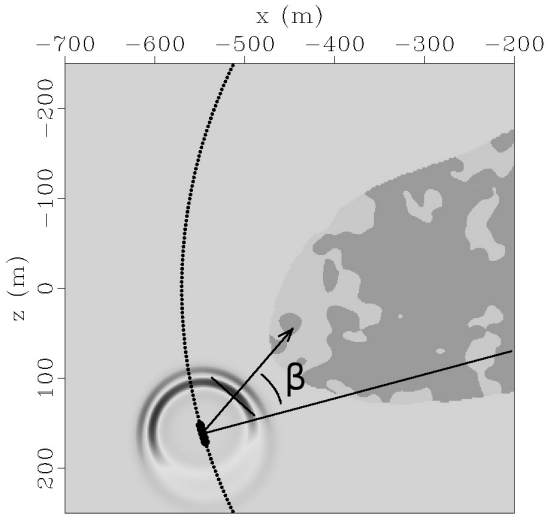

Figure 6: Synthetic aperture setup, using 5 source points as represented by the closely spaced thick dots (as referred to as $\mathbf{r}_p$). Indicated is the traveling direction of the maximum amplitude, described by the angle β. Setup shown for a specific location, 197° relative to the target (as defined in figure 3).

2.4.2 Receiver-side

Similar to the source side waveform SAR, the slant stacking processing technique can be done on the receiver side as well, changing the receiver wavefield.

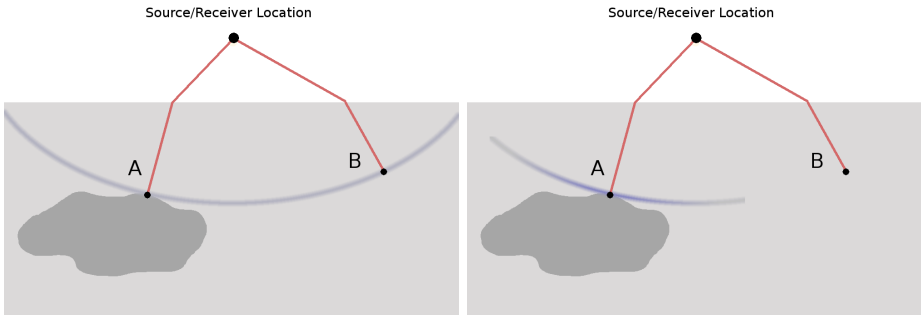

(a) Single (b) Waveform SAR

Figure 7: Illustration showing the imaging benefit of Waveform SAR. The blue arc represents a migrated image of the first arrival of an arbitrary scattering object underneath the surface.

Receiver-side waveform SAR represents an experimental setup where a EM pulse is emitted from a point source (at location $\mathbf{r}_s$=$\mathbf{r}_r$), but data recorded for multiple directions. Similar to source-side SAR, in practice this could be done by a radar dish which amplifies signals depending on the angle (β) of the dish. This analogue situation is represented by again slant stacking data in an array ((at locations $\mathbf{r}_p$)) along recording loation $\mathbf{r}_r$. The amplified/slant stacked data at $\mathbf{r}_r$ is given by:

$$D_{r\ point}(\mathbf{r}_r, \beta, \tau) = \sum_p G_p\big(\mathbf{r}_p,\ t + \Delta t_{p,\beta} \mid \mathbf{r}_r, t\big) \tag{11}$$

Where τ is the intercept time, the time dimension of the stacked data. The receiver wavefield as described in equation 6 is produced propagating data from all points in the array $\mathbf{r}_p$. The data at array locations $\mathbf{r}_p$ is based on the data the recording location $\mathbf{r}_r$, but time shifted by Δt in equation 10 to constructively interfere in the direction β.

$$D_{r\ array}(\mathbf{r}_p, \beta, t) = D_{r\ point}(\mathbf{r}_r, \beta, \tau + \Delta t_{p,\beta}) \tag{12}$$

3 Simple model

Receiver-and source-side waveform SAR are very similar in the way they improve image quality. This is illustrated in figure 7. When using data of a single shot (zero-offset), a first arrival of the data trace will be imaged along an ellipse (7a). This is because from this data alone, we cannot know if the signal originated from a scatter at point A; it may lie on point B as well or any other point along the arc. However, with waveform SAR, this can be narrowed down to a rough direction (7b).

In order to better demonstrate the benefits of using waveform SAR, I employ SAR on a simple model which will showcase any artifacts better than the more complicated asteroid model. The geometry of this simple model consist of a point scatter in an otherwise constant velocity field. Shot & receiver locations are located in a line as shown in figure 8. Resulting images by migration using zero-offset data, source-side SAR and receiver-side SAR are shown in figure 9. SAR is employed here using 9 point sources, which equals an array length of 22.5 meters. Results are shown for a finely sampled case and and coarsely sample case. In the finely sampled case, migration is preformed at all location points (there is no undersampling). In the coarse case, the image is the result undersampling, where migration was preformed using only 7 points for the whole imaging domain.

The results in figure 9 show that the images are different in amplitude for the coarse case, but nearly the same for finely sampled case. Shown is source-side waveform SAR only, because the result for receiver-side waveform SAR is (almost) the same. All images produced by coarse sampling show clear artifacts, because the artifacts in the images at every shot location were not finely sampled enough to deconstructively interfere. But magnitude of the artifacts is smaller when SAR is employed, clearly visibly when the two coarsely sampled images are subtracted from each other, as done in figure 10. The magnitude of artifacts in figure 10 is shown as a fraction of the amplitude of the scatter (set to 1). Thus waveform SAR significantly attenuated artifacts when the imaging domain is coarsely sampled.

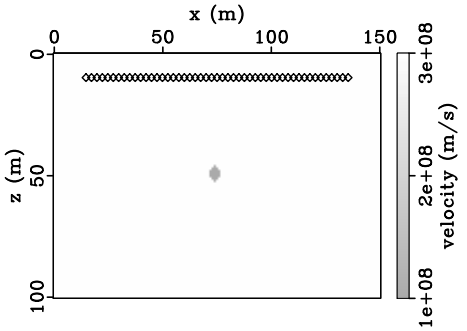

Figure 8: Model setup. Velocity model is a constant media with a point a sharp anomaly in the middle of the domain. The line of diamond symbols represents record & shoot locations

4 Slant stacked data

The slant stacking of data for source-side waveform SAR as described by equation 9 is visualized for a specific shot/record location in figures 11 and 12. Figure 11 shows the data at a specific location as a function of time and of shot loca-

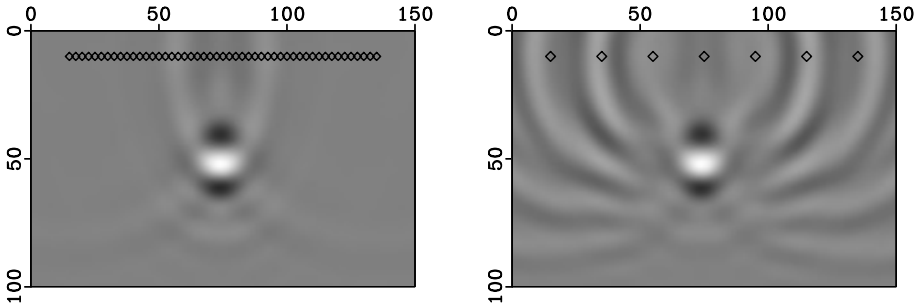

(a) Single, fine sampling

(b) Single, coarse sampling

(c) waveform SAR, fine sampling

(d) waveform SAR, coarse sampling

Figure 9: Migration results for the simple model shown in figure 8. Results are shown for migration of zero-offset data, referred to as 'single', and migration of using waveform SAR. Left side shows fine sampling, right side coarse sampling, referring to the number of location used for migration

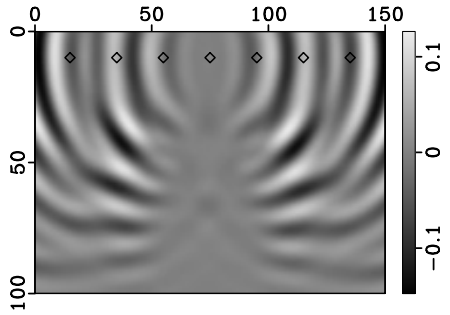

Figure 10: Artifact comparison of waveform SAR for simple model (fig 8). Shown is the difference between 9b and 9d. Amplitude is a given as a fraction of the maximum amplitude of the scatter imaged in 9a.

tion (denoted by the location angle α on the x-axis, see figure 3). I will refer to the domain of figure 12 as the intercept time - direction domain, τ-β, because

of the similarity to the τ-p transform (Stoffa 1981). In the τ-p transform, ray parameter p corresponds to an incidence angle, with is analogue to the case presented here where β represents the angle of the incoming or outgoing direction of maximum interference of the wavefield.

In figure 13, τ-β data is plotted with 4 different array lengths. This is denotet by 3 equivalent measures, the array's actual length, amount point sources used and angle range (for clarity, see the small overviews wit in the figures of 13). For better visualization of the later arrivals, the signals are amplified by a gain of factor t.

Figure 13 confirms that the information contained in the data in the τ-β domain clearly decreases with smaller amount of source points, with the data being smeared out on the angle axis. However, as visible in figure 13c, we see that there is still information while using few source points: for example, one can see that the signal is stronger off-center. This corresponds to the general location of the asteroid relative to the satalite location. Thus migration of the data contained in figure 13c should at least amplify the image near true scatter point and attenuate signals further away from the target.

Migration should be preformed with finer angle sampling when the figure shows large, small wavelength variation on the angle-axis, in order to avoid aliasing of the image after migration. Certain direction ranges have a larger contribution to the image due a higher signal amplitude in the τ-β domain. However, this is unlikely to be known in advance when data is shot in practice, in contrast to the processing method using point sources presented here. Another important note is that migration using finer angle sampling will also in increase computational cost. In the next section migration results are presented, and considering the data in figures 13, the computation cost and available means, waveform SAR migration will be preformed using 21 source points and 5 directions (angles -40° ,-20° ,0° ,20° and 40°).

5 Migration results

Figure 14 shows the result using waveform SAR with an array size of 21 point sources. This is chosen based on the figures 13, although this array size, equivalent to 120 meters, may be unrealistic compared to real antenna setups such as the 40 meter boom of the MARSIS experiment (Jordan, R., et al 2009). To asses the quality of the image objectively, I compare it with the image produced by using full acquisition, as shown in figure 5e. In order to compare images, they are clipped at half the maximum value, and scaled. Then the images are subtracted from the best image (using true velocity, full acquisition) and the L2 norm is computed. Because the image within the asteroid is of interest, any contribution to the norm value outside the asteroid is ignored. The result is summarized in table 2. A striking result is that the norm of migration by zero-offset data referred to as 'single' in the table, shows a reasonably accurate result when finely sampled ($0 < \text{norm} < 1$), but becomes poor when coarsely

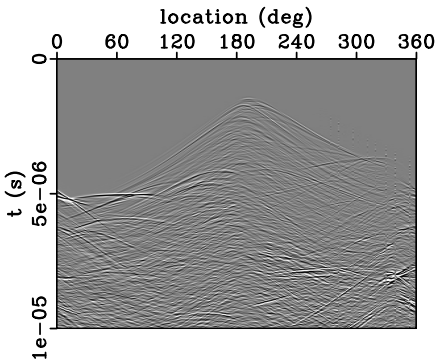

Figure 11: Receiver gather at location ≈187°, with source location denoted by angle relative to the target, see figure 3. Later arrivals amplified by a factor t.

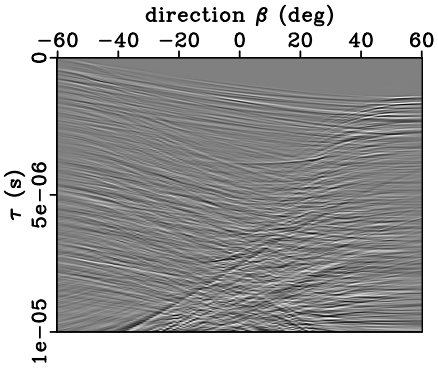

Figure 12: Transformed data of figure 11 to the τ-β domain (for arc length of 242.0°.

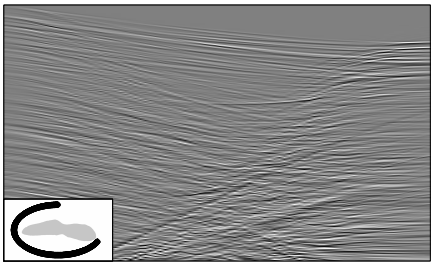

(a) 401 pnts, 2400 m, 242.0°

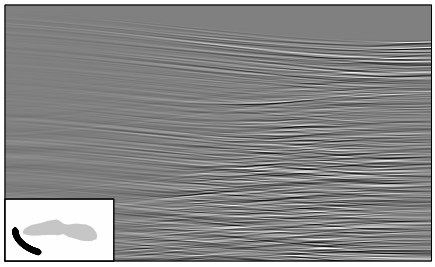

(b) 101 pnts, 600 m, 60.5°

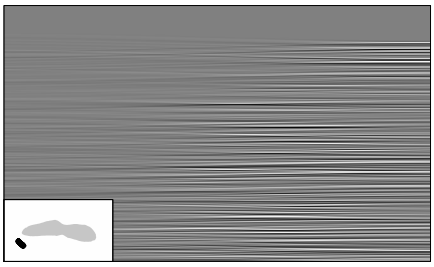

(c) 21 pnts, 120 m 12.1°

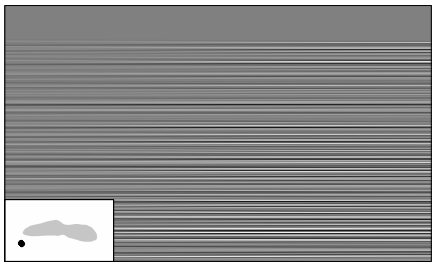

(d) 5 pnts, 24 m, 2.42°

Figure 13: Intercept time - direction (τ-β) plot for a receiver located at ≈187° relative to the target. Indicated is the amount of sourcepoints used, the corresponding arc array length, and the corresponding angle range. Plots show time-angle domain, same axes as figure 12

sampled (norm > 1). This is in contrast to imaging using waveform SAR, where the relative norm value stays below 1.

Table 2: Relative norm of images compared to the best image (true velocity, full acquisition)

model	fine	coarse
single	.918	1.226
source-side SAR	.904	.988
receiver-side SAR	0.874	0.960

6 Discussion

Table 2 shows that the images using waveform SAR are only slightly better than using zero-offset data when finely sampled, but much better when coarsely sampled. This originates from the fact that waveform SAR can yield a better image for single shots. However, when stacked over many finely spaced shots, artifacts deconstructively interfere, rendering waveform SAR less useful. This conclusion is consistent with the results of a simple model (figure 9).

Migration using waveform SAR has an higher computational cost per migration lcoation. The actual computation cost depends on if it's done source or receiver side. Source-side waveform SAR requires computation of receiver wavefield for every angle at all locations. The source wave-field however, requires an amount of wave simulations proportional to either the number of angles (N_{ang}) used or number of source points (N_p) used. The total computations per location is thus $N_{ang} + min(N_{ang}, N_p)$.

The reason the receiver wavefields can be computed using multiple methods is that the wave operator is linear, thus the field is the sum of individual contributions. The invidual contributions only need to be computated once, which is analogue to the with the conclusion of plane-wave depth migration of Stoffa et al. (2006). The following 2 formulations for the source wavefield show this inherent linearity:

$G_\beta^{Sou}(\mathbf{x}, t) = \sum_p G_p\big(\mathbf{x},\ t + \Delta t_{p,\beta} \mid \mathbf{r}_p, t\big)$ — Point source response is computed, then wavefields are time-shifted and stacked for every angle β

$G_\beta^{Sou}(\mathbf{x}, t) = G\big(\mathbf{x},\ t \mid \mathbf{r}_{all\ p's}, t{+}\Delta t_{p,\beta}\big)$ — Wavefield is calculated directly, but requires wavefield simulation for every angle β

Here, $\Delta t_{p,\beta}$ is the time shift (equation 10) for specific angle β and source point p, and $r_{all\ p's}$ denotes that (time-shifted) sources are injected as a bound-

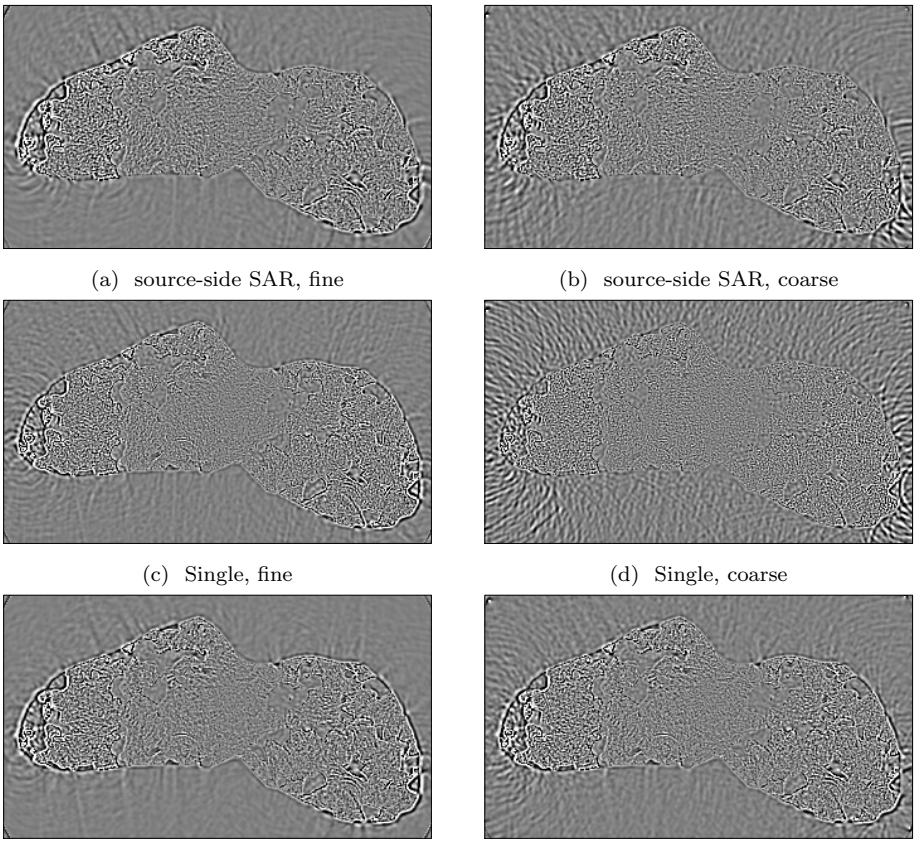

(a) source-side SAR, fine

(b) source-side SAR, coarse

(c) Single, fine

(d) Single, coarse

(e) receiver-side SAR, fine

(f) receiver-side SAR, coarse

Figure 14: Top: images using source-side waveform SAR. Middle: Images single, referring to migration using zero-offset data. Bottom: images using receiver-side waveform SAR. Left: finely sampled with 5 locations per wavelength (no undersampling). Right: coarsely sampled, 1 location per 2 wavelengths (60m)

ary condition into the wave propagator at all array locations instead of one location.

The computational cost for receiver-side waveform SAR is considerably lower: The source wavefield is indifferent with respect to angle β, thus requiring only 1 wave simulation per location. The total receiver-side waveform SAR is thus $min(N_{ang}, N_p) + 1$ per shot location.

Combining source- & receiver-side waveform SAR may improve image quality (even) more. However this will increase computational cost significantly as well, depending on the amount of angles used. Quantifying the image improvement of combining source- & receiver-side waveform SAR may a topic of further research.

7 Conclusion

In this paper, using a synthetic model of an asteroid, radar imaging by migration of slant stacked data is preformed, referred to as Waveform Synthetic Aperture Radar (waveform SAR). Waveform SAR is computed on both the source- and receiver-side, but results are very comparable. The waveform SAR method is compared to imaging with zero-offset data as well as multi-offset data. The concept of waveform SAR is also demonstrated with a simple model, it's results are in agreement with the larger synthetic asteroid model. Waveform SAR shows better image quality than zero-offset migration, most notably when the target is coarsely sampled. This is because the image using SAR is more accurate per shot location, due to amplification of signals near the true location of scatterers.

8 References

A'Hearn et al. 'Deep impact: excavating comet Tempel 1.' in: Science 310.5746 (2005): 258-264.

Baysal, Edip, Dan D. Kosloff, and John WC Sherwood, 1983. 'Reverse time migration.' In: Geophysics 48.11 (1983) p1514-1524.

Carey et al. 'Finite difference time domain simulation of radar wave propagation through comet nuclei dielectric models' in: Meteoritics & Planetary science (2008) 43, p:1085-1095

Chapman, C., 2004, 'The hazard of near-Earth asteroid impacts on Earth'. In: Earth Planet. Sci. Lett. 222, 1–15.

Claerbout, J.F., 1985. 'Imaging the Earth's Interior', publisher: Blackwell Scientific Publications.

Fleury & Vasconcelos, 2012, 'Imaging condition for nonlinear scattering-based imaging: Estimate of power loss in scattering' in: Geophyscis Vol 77 No 1

Graps et al. 2016, In-space utilisation of asteroids: "Answers to Questions from the Asteroid Miners", White Paper from the Asteroid Science Intersections with In-Space Mine Engineering (ASIME)

Griffiths, 2008, 'Introduction to electrodynamics', publisher: Prentice Hall

Grimm et al. 2014, 'Radio reflection imaging of asteroid and comet interiors II: Results and recommendations', in: Advances in space research 55 (2015) 2166-2176

Ittharat D. 2014,'3D Radio reflection imaging of asteroid interiors', MSC. Thesis, Colorado School of Mines

Jordan, R., et al 2009. 'The Mars express MARSIS sounder instrument.' In: Planetary and Space Science 57.14-15 (2009): p1975-1986.

Kofman et al. 2015, 'Properties of the 67P/Churyumov-Gerasimenko interior revealed by CONSERT radar', in: Science (2015) vol 349 issue 6247

Ladyzhenskaya, O. A. 1985. 'The Method of Finite Differences'. In: The Boundary Value Problems of Mathematical Physics (pp. 212-307). Springer, New York, NY.

Safaeinili et al. 2002, 'Probing the interior of asteroids and comets using radio reflection tomography' in: Meteoritics & Planetary science (2002) 37, p:1953-1963

Sava et al. 2014, 'Radio reflection imaging of asteroid and comet interiors I: Acquisition and imaging theory', in: Advances in space research 55 (2015) p:2149-2165

Seu, Roberto, et al 2007. 'SHARAD sounding radar on the Mars Reconnaissance Orbiter.' In: Journal of Geophysical Research: Planets 112.E5 (2007).

Skolnik, 1970, 'Radar Handbook', publisher: McGraw-Hill. Chapter 1 & 21

Stoffa et al. 2006. 'Plane-wave depth migration'. In: Geophysics VOL. 71 NO. 6 p261-272

Stoffa et al. 1981 'Direct mapping of seismic data to the domain of intercept time and ray parameter -A plane-wave decomposition'. In: Geophysics VOL. 46 NO. 3 p255-267